


Mobility edge of Stark many-body localization

Li Zhang ^{1,2} Yongguan Ke ^{1,3,*} Wenjie Liu,^{1,2} and Chaohong Lee ^{1,2,†}

¹Guangdong Provincial Key Laboratory of Quantum Metrology and Sensing & School of Physics and Astronomy, Sun Yat-Sen University (Zhuhai Campus), Zhuhai 519082, China

²State Key Laboratory of Optoelectronic Materials and Technologies, Sun Yat-Sen University (Guangzhou Campus), Guangzhou 510275, China

³Nonlinear Physics Centre, Research School of Physics, Australian National University, Canberra Australian Capital Territory 2601, Australia

 (Received 21 September 2020; revised 26 January 2021; accepted 29 January 2021; published 22 February 2021)

We investigate many-body localization of interacting spinless fermions in a one-dimensional disordered and tilted lattice. The fermions undergo *energy-dependent transitions* from ergodic to Stark many-body localization driven by the tilted potential, which are manifested by the appearance of mobility edges between delocalized states and Stark many-body localized states even when the disorder is weak. We can concretely diagnose these transitions rather than crossovers by finite-size scaling of energy-level statistics. Moreover, in the Stark many-body localization, the entanglement entropy obeys the area law scaling, in analogy to that in the conventional many-body localization.

DOI: [10.1103/PhysRevA.103.023323](https://doi.org/10.1103/PhysRevA.103.023323)

I. INTRODUCTION

Mobility edge, a critical value separating delocalized and localized states in energy spectrum, has been extensively studied since the seminal work of Anderson localization [1,2]. Marking a true quantum phase transition, single-particle mobility edge can exist in three-dimensional random disorder and lower-dimensional quasiperiodic potential [3–12]. Theoretically, the mobility edge can be determined by the extension or the inverse participation ratio of the wave function of the eigenstates [8–11]. In experiments, the mobility edge has been measured for noninteracting ultracold atoms in a three-dimensional disordered and a one-dimensional quasiperiodic potential [5,6,12].

Localization of particles in disorder persists even in the presence of interactions, now known as many-body localization (MBL), which serves as a robust mechanism for ergodic breaking in isolated quantum systems [13–16]. Similar to Anderson transition, there may also exist a mobility edge separating many-body localized and ergodic states [17,18]. MBL has significantly distinct features from ergodic phases, such as logarithmic growth versus ballistic growth of entanglement from nonentangled initial condition [19–22], area law versus volume law scaling of entanglement entropy (EE) [15–17,23–25], and Poisson distribution versus Wigner-Dyson distribution of energy level spacings [17,26–28], which can apply to determine the mobility edge. Important experimental progress has also been made in exploring the MBL in various platforms involving ultracold atoms, trapped ions, nuclear spins, and superconducting circuits [29–39].

However, disorder is not the essential ingredient for MBL, e.g., a static field may also provide a robust mechanism to induce MBL, which is named as Stark MBL [40,41]. In closed systems, the Stark MBL shares analogous nonergodic behaviors with the conventional disorder-induced MBL [40–42], such as the Poisson statistic distribution of energy level spacings and the logarithmic growth of entanglement. A further study shows that the Stark MBL can be distinguished from the conventional MBL via the entanglement growth when the systems are coupled to an external dephasing bath [43]. It is natural to ask whether the mobility edge exists for interacting particles in a tilted and disordered lattice where Stark MBL is present. Recently, the authors of Ref. [44] found a broad crossover from the ergodic phase to the localized phase as the tilted potential increases. However, evidence of an *energy-dependent transition* from the ergodic phase to the Stark MBL is still lacking.

In this article, we explore the ergodic-Stark MBL transition of interacting spinless fermions in a one-dimensional optical lattice subjected to uniform field and disorder, as depicted in Fig. 1. We calculate the eigenspectrum and eigenstates in an energy-resolved way by using a shift-inverse exact diagonalization method. We uncover a clear mobility edge through analyzing the statistics of the eigenspectrum and finite-size scaling. Furthermore, we study the entanglement structure of the eigenstates and find that the EE obeys the area law scaling in the Stark MBL.

The rest of the article is organized as follows. In Sec. II, we introduce the model for our physical system. In Sec. III, we analyze the spectral properties and obtain the phase diagram. In Sec. IV, we analyze the entanglement properties of the Stark MBL phase. In Sec. V, we conclude and discuss our results.

*keyg@mail2.sysu.edu.cn

†lichao2@mail.sysu.edu.cn

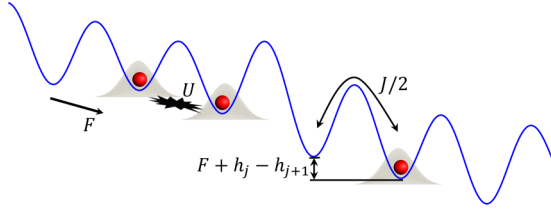


FIG. 1. Schematic diagram of the interacting spinless fermions in a disordered lattice subjected to a uniform field with strength F . The fermions interact through nearest-neighbor interaction U and tunnel between nearest sites with strength $J/2$.

II. DISORDERED STARK LADDER OF INTERACTING SPINLESS FERMIONS

We consider an ensemble of interacting spinless fermions in a one-dimensional disordered lattice in the presence of a uniform field; see Fig. 1, which is described by the Hamiltonian

$$\hat{H} = \sum_{j=1}^{L-1} \left[\frac{J}{2} (\hat{c}_j^\dagger \hat{c}_{j+1} + \hat{c}_{j+1}^\dagger \hat{c}_j) + U \hat{n}_j \hat{n}_{j+1} \right] + \sum_{j=1}^L V_j \hat{n}_j. \quad (1)$$

Here, the system size is finite with total number of sites L . \hat{c}_j^\dagger (\hat{c}_j) creates (annihilates) a fermion at site j and $\hat{n}_j = \hat{c}_j^\dagger \hat{c}_j$ is the particle number operator. $\frac{J}{2}$ and U are the nearest-neighbor tunneling and interaction strength, respectively. $V_j = h_j - Fj$ is the position-dependent potential, where F is the strength of the uniform field and $h_j \in [-W, W]$ is uniformly distributed with disorder strength W . The energy unit is set as $J = U = 1$. In the absence of disorder and at the single-particle level, the eigenstates are the well-known Wannier-Stark states and the energy spectrum forms an equidistant ladder, namely the Stark ladder [45–47]. The Stark ladder causes exact many-fold degeneracies in the many-body energy spectrum, which can be lifted by the disorder to recover the generic localization behaviors [41,42].

We consider half-filling of the lattice with total particle number $N = L/2$ in the open boundary condition. By the exact diagonalization method, we study such a system in different sizes by averaging different disordered configurations: $L = 12$ (at least 2000 samples), 14 (1000 samples), 16 (1000 samples), and 18 (600 samples). Using the shift-invert spectral transformation $(\hat{H} - E\hat{I})^{-1}$ with \hat{I} being the identity matrix, we can reach eigenstates at any energy density $\epsilon = (E - E_{\min})/(E_{\max} - E_{\min})$ [17], where E_{\min} and E_{\max} are the minimum and maximum eigenenergies for each disorder realization, respectively. In the following studies, we consider $\epsilon \in [0.15, 0.85]$ since the densities of states are too low at the high- and low-energy tails of the energy spectrum. For each parameter point and each disorder realization, we take the closest 50 eigenpairs around each ϵ . The observables are calculated from the corresponding eigenstates and averaged over the set of eigenpairs and disorder realizations.

III. MANY-BODY MOBILITY EDGE INDUCED BY UNIFORM FIELD

A well-known criterion to distinguish the MBL from the ergodic phase is the statistic of the many-body eigenspectrum.

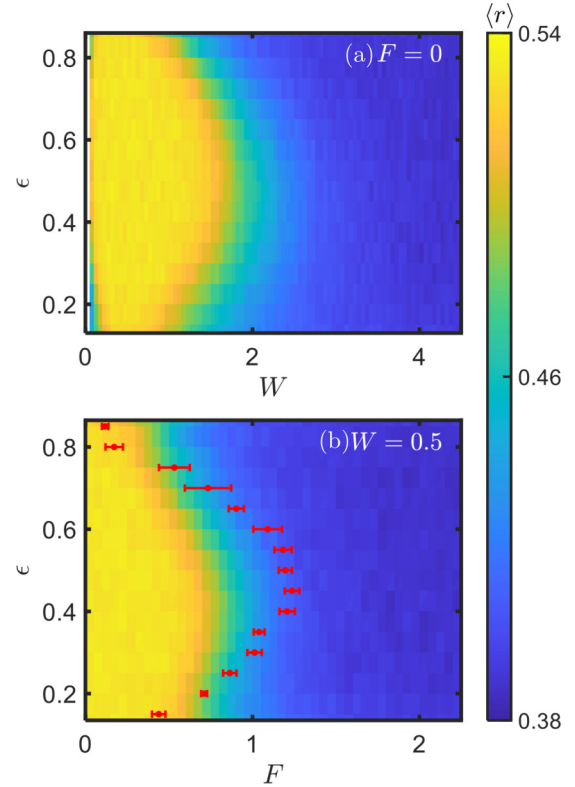


FIG. 2. (a) The disorder-averaged ratio of energy level spacings $\langle r \rangle$ as a function of (ϵ, W) at $F = 0$. In the weak disorder region, all the eigenstates are ergodic. (b) $\langle r \rangle$ as a function of (ϵ, F) at $W = 0.5$. The colors denote the values of $\langle r \rangle$ at $L = 16$. The numerical data marked by red dots are the critical points extracted from the finite-size scaling of $\langle r \rangle$ at system sizes $L = 12, 14, 16$, and 18 . The error bars represent the standard deviation from different fitting windows and trials in the scaling process, see the text. The energy unit is set as $J = U = 1$.

The ratio of the adjacent energy gap is defined as

$$r_n = \min(\delta_{n+1}/\delta_n, \delta_n/\delta_{n+1}), \quad (2)$$

with $\delta_n = E_n - E_{n-1}$ being the energy gap between eigenenergy E_{n-1} and E_n . In the many-body localized system such ratio obeys the Poisson distribution, $P_P(r) = 2/(1+r)^2$, while in the ergodic system it obeys the Wigner-Dyson distribution of Gaussian orthogonal ensembles, $P_{\text{GOE}}(r) = 8(r+r^2)/27(1+r+r^2)^{2.5}$ [48]. It is convenient to use $\langle r \rangle$, the average of the adjacent gap ratio over different disorder realizations, to distinguish the two phases. $\langle r \rangle$ changes from $\langle r \rangle_P \approx 0.386$ in the localized phase to $\langle r \rangle_{\text{GOE}} \approx 0.531$ in the ergodic phase. In the absence of the field, all the eigenstates are ergodic when $W \lesssim 1.8$ [17]. In Fig. 2(a), we show how the disorder-averaged ratio $\langle r \rangle$ changes with energy density and disorder strength at $F = 0$ and system size $L = 16$. We numerically checked the values of $\langle r \rangle$, and find that $\langle r \rangle \approx \langle r \rangle_{\text{GOE}}$ for all energy densities when $0.1 \lesssim W \lesssim 1$. The small nonergodic region in the lower-left corner in Fig. 2(a) is most probably due to the proximity to the integral point $W = 0$ [26]. Without loss of generality, in the following study we fix $W = 0.5$, at which all the eigenstates at $F = 0$ are ergodic,

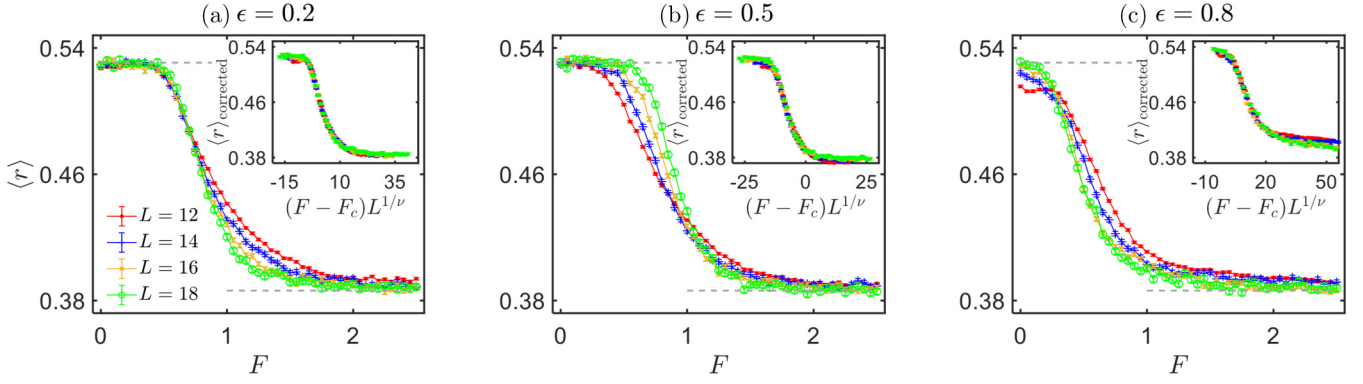


FIG. 3. The disorder-averaged ratio of the consecutive level spacings $\langle r \rangle$ as a function of the field strength at different energy densities (a) $\epsilon = 0.2$, (b) $\epsilon = 0.5$, and (c) $\epsilon = 0.8$. The data at system sizes $L = 12, 14, 16$, and 18 are denoted by red lines marked by dots, blue lines marked by pluses, yellow lines marked by crosses, and green lines marked by circles, respectively. The two dashed gray lines correspond to $\langle r \rangle_{\text{GOE}}$ and $\langle r \rangle_{\text{P}}$, respectively. The error bars stand for the standard error, which is smaller than the symbol size. Inset: Collapse of the corrected data with $(F_c, \nu, y, g_{10}) =$ (a) $(0.74, 0.92, -2.41, 3.67)$; (b) $(1.27, 0.94, -2.09, 3.21)$; (c) $(0.16, 0.80, -2.18, -3.22)$. The energy unit is set as $J = U = 1$.

and explore whether the uniform field will induce the transition from the ergodic phase to the localized phase.

In Fig. 2(b), we show the distribution of the disorder-averaged gap ratio $\langle r \rangle$ in the plane of (F, ϵ) at $W = 0.5$ and $L = 16$. It is obvious that for all the energy densities, $\langle r \rangle$ crossovers from $\langle r \rangle_{\text{GOE}}$ to $\langle r \rangle_{\text{P}}$ as the strength of the field increases, which indicates that there may be a transition from the ergodic phase to the Stark MBL. Moreover, there also exists crossover from the ergodic phase to the localized phase as energy changes, which indicates the possible existence of a mobility edge.

To ascertain the energy-dependent ergodic-Stark MBL transition and the critical points, we perform finite-size scalings of $\langle r \rangle$ for different energy densities, and the system sizes are chosen as $L = 12, 14, 16$, and 18 . In Fig. 3, we plot $\langle r \rangle$ as a function of F at energy densities $\epsilon = 0.2, 0.5$, and 0.8 . As the strength of the field increases, the values of $\langle r \rangle$ for different system sizes cross around a critical value F_c between the two limiting values $\langle r \rangle_{\text{GOE}}$ and $\langle r \rangle_{\text{P}}$. The critical points F_c can be extracted via rescaling F by $(F - F_c)L^{1/\nu}$, so that the data of $\langle r \rangle$ collapse into a single universal function of $(F - F_c)L^{1/\nu}$. However, the finite system size causes the crossing point shift with the system size, which is rather obvious in Fig. 3(b).

To estimate the values of the critical uniform field strength F_c under the condition of limited system sizes, we express the scaling function of the averaged gap ratio $\langle r \rangle$ as

$$r = g(\chi L^{1/\nu}, \phi L^y), \quad (3)$$

where χ is the relevant scaling variable, ν is the critical exponent, and ϕL^y is the irrelevant correction term to the scaling, which accounts for the shift of the critical point F_c with system size. The relevant and irrelevant variables χ and ϕ can be expanded in terms of F as

$$\begin{aligned} \chi &= (F - F_c) + \sum_{k=2}^{m_R} \chi_k (F - F_c)^k, \\ \phi &= 1 + \sum_{k=1}^{m_I} \phi_k (F - F_c)^k. \end{aligned} \quad (4)$$

Expanding in a Taylor series of the irrelevant variable [49,50], the scaling function reads as

$$r = \sum_{k=0}^{m_I} (\phi L^y)^k g_k(\chi L^{1/\nu}) = g_0(\chi L^{1/\nu}) + \phi L^y g_1(\chi L^{1/\nu}) + \dots, \quad (5)$$

where $g_{k>0}$ are the correction functions due to the irrelevant variable. Each $g_k(\chi L^{1/\nu})$ can be a Taylor series of $\chi L^{1/\nu}$:

$$g_k(\chi L^{1/\nu}) = \sum_{l=0}^{n_k} g_{kl}(\chi L^{1/\nu})^l, \quad (6)$$

where g_{kl} are the variables of different orders. The order of expansions in Eqs. (4) and (6) should be restricted by $m_R \geq m_I$ and $n_0 \geq n_1 \geq \dots$ since the irrelevant term is less important than the relevant one in the scaling function and it should be less important as the order of correction increases [50]. The correction should vanish in large L , thus the irrelevant exponent $y < 0$. The scaling of $\langle r \rangle$ is exhibited by subtracting the correction terms such that the corrected data

$$r_{\text{corrected}} = \langle r \rangle - \sum_{k=1}^{m_I} (\phi L^y)^k g_k(\chi L^{1/\nu}) \quad (7)$$

collapse into a single universal function $g_0(\chi L^{1/\nu})$. Here, we suppose nonlinearity is absent in the expansion of χ and only the constant term is kept in the expansion of ϕ , that is, $m_R = 1$ and $m_I = 0$.

There are totally $N_p = (m_R - 1) + m_I + \sum_{k=1}^{n_1} (n_k + 1) + 3$ free fitting parameters when the correction is present and $N_p = (m_R - 1) + 2$ free parameters when the correction is absent. We consider corrections up to the first order (with $n_1 = 1$ and $n_1 = 0$). The details of our finite-size scaling procedure are referred to the Appendix. We find that comparing to that without correction, including the first-order correction improves the degree of data collapse by reducing the difference of the rescaled curves \mathcal{D} (see Fig. 6) and eliminates the shift of the critical field strength (see Fig. 7). The collapse of the corrected data is respectively shown in the insets of Fig. 3, where $\langle r \rangle_{\text{corrected}}$ for all system sizes collapse into a single function $g_0[(F - F_c)L^{1/\nu}]$. Proceeding with higher

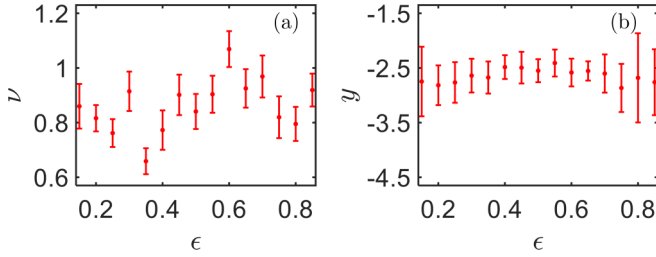


FIG. 4. (a) The critical exponents ν and (b) the irrelevant exponents at different ϵ . The error bars represent the standard deviation.

orders of correction is straightforward, but we do not perform them further since \mathcal{D} is reduced less than one order for the first-order correction.

The critical values for different energy densities after the first order of correction are plotted in Fig. 2(b) (see the red dots with error bars), which shows a clear mobility edge induced by the uniform field. We notice that this mobility edge is asymmetric about the center of the energy spectrum: it is slightly shifted towards the ground energy, which resembles that in the disordered many-body systems [17,18]. The critical exponent and the irrelevant exponent are shown in Fig. 4. The results give a consistent value of the critical exponent for all the ϵ with $\nu = 0.86 \pm 0.12$, and a consistent value of the irrelevant exponent with $y = -2.64 \pm 0.43$. We notice that the error bars of y are relatively large at the boundaries of ϵ , which may be attributed to the lower density of states at the tails of the energy spectrum.

IV. AREA LAW OF ENTANGLEMENT ENTROPY

At last, we study the entanglement properties of the many-body eigenstates in the ergodic phase and the Stark MBL. The bipartite entanglement between a subsystem A and the rest of the system B can be quantified by the von Neuman EE

$$S = -\text{Tr}(\hat{\rho}_A \ln \hat{\rho}_A), \quad (8)$$

where $\hat{\rho}_A$ is the reduced density matrix of the subsystem A . We consider the half-chain EE, i.e., the subsystem A is chosen to be a block of $\frac{L}{2}$ contiguous sites. In our calculation, the eigenstates are expressed in the Fock bases as $|\psi\rangle = \sum_{n_1, \dots, n_L} C_{n_1, \dots, n_L} |n_1 \dots n_L\rangle$, where $n_i = 0, 1$ is the number of particles on site i and C_{n_1, \dots, n_L} is the complex amplitude. The reduced density matrix of the subsystem A then reads

$$\hat{\rho}_A = \sum_{\vec{n}_L, \vec{n}'_L} |\vec{n}_L\rangle \langle \vec{n}'_L| \sum_{\vec{n}_R} C_{[\vec{n}_L, \vec{n}_R]} C_{[\vec{n}'_L, \vec{n}_R]}^*, \quad (9)$$

where $\vec{n}_L = \{n_1 \dots n_{L/2}\}$ and $\vec{n}_R = \{n_{L/2+1} \dots n_L\}$ are shorted for the sequence of occupation numbers of the left and right parts of the chain. According to the above reduced density matrix, we can calculate the von Neuman EE for different parameters and disorder realizations. In the ergodic phase, the eigenstates are thermal, thus the von Neuman EE equals to the thermodynamic entropy, which is extensive. This leads to the volume law scaling of the von Neuman EE, that is, S is proportional to the volume of the subsystem A [15,16]. In the disorder-induced MBL, the eigenstates can be written as product states by quasilocality unitary transformations, which

implies that the von Neuman EE is proportional to the area of the surface between the two subsystems, that is, it obeys the area law scaling [15–17,23–25].

EE has been calculated in tilting systems [51,52], but the analysis of the scaling of EE with system size is still lacking. We now test the volume law and area law scalings of the EE in the ergodic phase and the Stark MBL, respectively. The disorder-averaged $\langle S \rangle$ is shown in Fig. 5, as a function of F at energy densities $\epsilon = 0.2, 0.5$, and 0.8 and different system sizes. In the ergodic phase at weak field strength, $\langle S \rangle$ is size-dependent and behaves as $L f_\epsilon(F) + c_\epsilon(F)$, signifying the volume law scaling. The maximum EE at each energy density approaches $\frac{L}{2} \ln 2 + c_\epsilon$, as shown by the dashed gray lines in Fig. 5. On the other hand, in the localized phase at strong field, the averaged EE is much lower than that in the ergodic phase and collapses into a single curve for all system sizes, meaning that the EE obeys the area law scaling in the Stark MBL.

In the insets of Fig. 5, we plot the variance of the EE $\sigma^2 = \langle S^2 \rangle - \langle S \rangle^2$ as a function of the field strength at energy densities $\epsilon = 0.2, 0.5$, and 0.8 . It is well known that for the ergodic-MBL transition, the variances of the EE in finite systems show peaks near the transition points, originating from the coexistence of the delocalized and localized regime [25], and can be used to locate the transition points [17,25]. We find that this scenario is also valid in the ergodic-Stark MBL transition, as can be seen in the insets of Fig. 5, where the peaks of the variance become sharper and the corresponding locations tend to the transition points as the system size increases.

V. CONCLUSION AND DISCUSSION

We revealed the existence of a mobility edge between ergodic and Stark MBL states of interacting spinless fermions in a disordered Stark ladder. We find that the spectral properties of the Stark MBL are in common with that of the conventional disorder-induced MBL. Specifically, the statistic of the adjacent gap ratio of the eigenspectrum is of Poisson type and the EE obeys the area-law scaling in the Stark MBL. Through a finite-size scaling of the adjacent gap ratio, we give the phase diagram of the mobility edge in the eigenspectrum.

Based on the present techniques of manipulating and detecting ultracold atoms in optical lattices, it is possible to verify the mobility edge of interacting fermions in the disordered Stark ladder. As a dynamical phase transition, the MBL transition is commonly detected via monitoring the quench dynamics from an initial low entropy product state, usually the charge density wave state with even lattice sites occupied [32–34]. Distinction between the ergodic and localized phases is drawn by checking the stationary value of the imbalance between the atom numbers on the even and odd lattice sites, which is zero for the ergodic phase and nonzero for the localized phase. Although previous experiments do not consider the energy dependence of the MBL transition, extension to detect the mobility edge is feasible as long as the Hamiltonian parameters and the initial states are well known [53]. In the same spirit of Ref. [53], the Stark many-body mobility edge in this paper can be probed by monitoring the quench dynamics of different initial Fock states with different energies, which are conserved during the time evolution. Our model (1) can be realized by loading

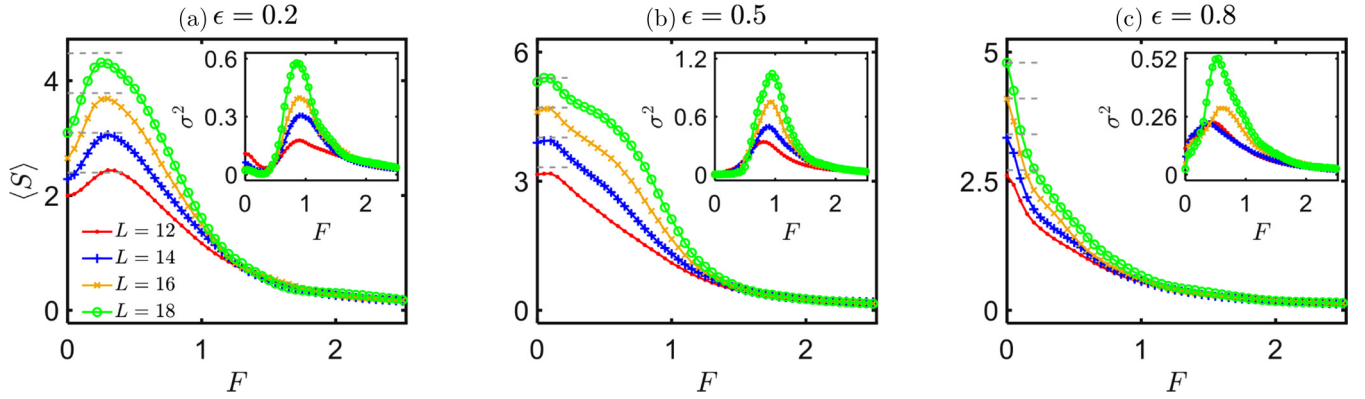


FIG. 5. The disorder-averaged von Neuman EE $\langle S \rangle$ as a function of the field strength F at different energy densities (a) $\epsilon = 0.2$, (b) $\epsilon = 0.5$, and (c) $\epsilon = 0.8$. The data at system sizes $L = 12, 14, 16$, and 18 are denoted by red lines marked by dots, blue lines marked by pluses, yellow lines marked by crosses, and green lines marked by circles, respectively. The dashed gray lines correspond to the maximal EE: (a) $\frac{1}{2} \ln 2 - 1.76$, (b) $\frac{1}{2} \ln 2 - 0.838$, and (c) $\frac{1}{2} \ln 2 - 1.445$. Insets: The disorder-averaged variance σ^2 of the von Neuman EE as a function of the field strength. The peaks become sharper as the system size increases and the peak locations indicate the ergodic-Stark MBL transition points. The energy unit is set as $J = U = 1$.

fermions in one-dimensional disordered and tilting optical lattices, with disorder created by an optical speckle field [54,55] and the tilt induced by a well-controlled magnetic field gradient. The disordered potential can be precisely measured and the localized single-particle wave function in the disordered lattice can be calculated [54,55]. Thereby, the Hamiltonian parameters can be determined with high precision. A generic initial Fock state with total particle number $L/2$ could be

precisely prepared with addressing technique [56]. The quench dynamics can be monitored via single-site and single-atom resolved fluorescence imaging [56–60]. All these techniques provide the possibility to probe the Stark many-body mobility edge.

Note added. Recently, we became aware of the related work of studying Stark MBL of bosons and the coexistence of localized and ergodic states in harmonic trap [61].

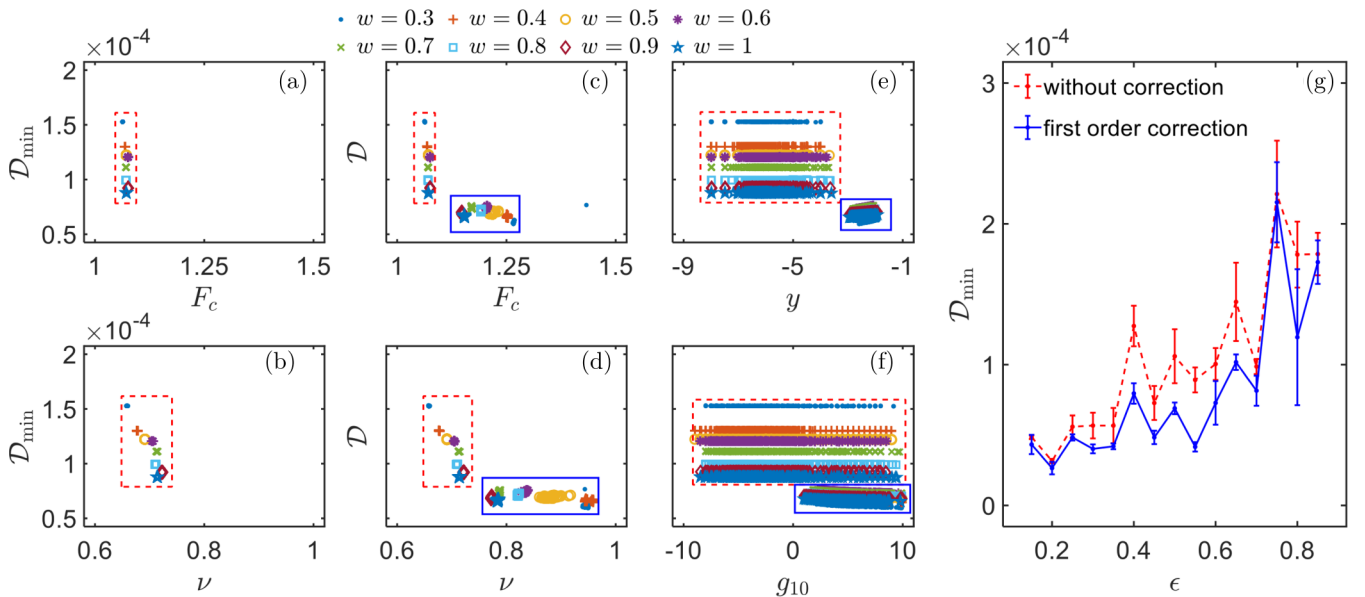


FIG. 6. (a, b) The global minima $\mathcal{D}_{\min}(F_c, \nu)$ of $\mathcal{D}(F_c, \nu)$ for different fitting windows at $\epsilon = 0.5$, when not considering corrections. The global minima for each w overlap in the space (F_c, ν) , such that each mark represents multiple sets of data. (c)–(f) The minima of $\mathcal{D}(F_c, \nu, y, g_{10})$ for different fitting windows at $\epsilon = 0.5$, when considering the simplest first-order correction ($n_1 = 1, n_1 = 0$). The data sets in the dashed red box represent the local minima for each w , which correspond to the global minima in (a) and (b). The data sets in the solid blue box represent the global minima for each w , which are used to estimate the critical points. The global minima in (e) and (f) are clustered tightly, such that the data in the blue box overlap with each other. (g) The global minima \mathcal{D}_{\min} at different ϵ without correction (dashed red line) and with the simplest first-order correction (solid blue line). The lines are guide to eyes. The error bars represent the standard deviation from different fitting windows and fitting trials.

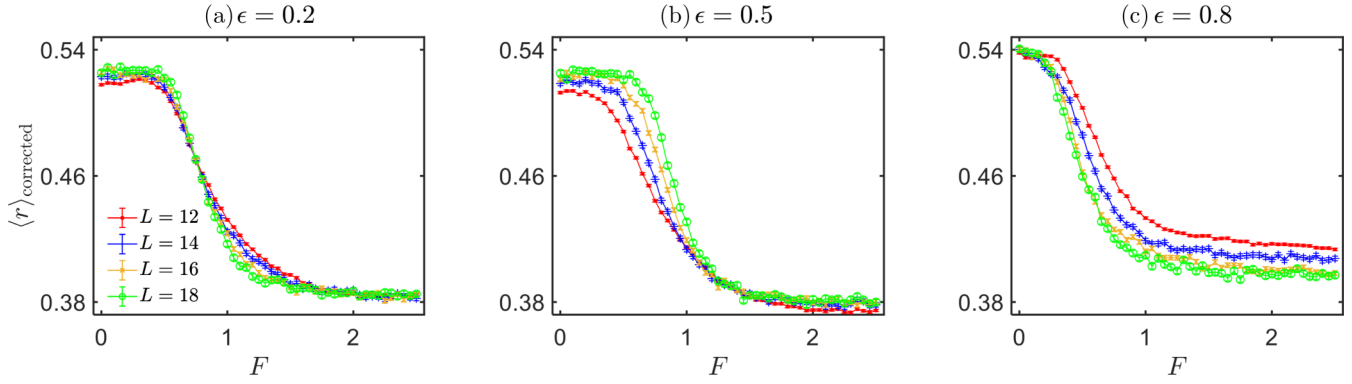


FIG. 7. The corresponding data in Fig. 3 after subtraction of the corrections for scaling [see Eq. (7)], with (F_c, ν, y, g_{10}) given by (a) (0.74, 0.92, -2.41, 3.67); (b) (1.27, 0.94, -2.09, 3.21); (c) (0.16, 0.80, -2.18, -3.22). The energy unit is set as $J = U = 1$.

ACKNOWLEDGMENTS

We thank Menghan Xia for useful discussion. This work is supported by the Key-Area Research and Development Program of Guangdong Province under Grant No. 2019B030330001, the National Natural Science Foundation of China (NNSFC) under Grants No. 11874434 and No. 11574405, and the Science and Technology Program of Guangzhou (China) under Grant No. 201904020024. Y.K. was partially supported by the Office of China Postdoctoral Council (Grant No. 20180052) and the National Natural Science Foundation of China (Grant No. 11904419).

APPENDIX: DETAILS OF FINITE-SIZE SCALING

To perform the collapse procedure, we define the difference of the rescaled curves between different system sizes as

$$\mathcal{D} = \frac{1}{wR} \sum_{L_i < L_j} \int_{-\frac{wR}{2}}^{\frac{wR}{2}} [r_{\text{corrected}}(x, L_i) - r_{\text{corrected}}(x, L_j)]^2 dx. \quad (\text{A1})$$

Here, $L_i = 12, 14, 16, 18$, $r_{\text{corrected}}(x, L_i)$ represents the spline-interpolated data of the corrected curve for each L_i after transforming F to $x = (F - F_c)L^{1/\nu}$, R is set as $\max[(F - F_c)12^{1/\nu}] - \min[(F - F_c)12^{1/\nu}]$, and w defines the width of the fitting window used for the collapse process. Thus, after setting w and the orders of expansion in Eqs. (5) and (6), \mathcal{D} is only a function of F_c, ν, y and other expansion coefficients \vec{g} as a combination of all g_{kl} for $k > 0$. Note that when not including the correction, \mathcal{D} only depends on F_c and ν . The critical values are obtained by minimizing \mathcal{D} . The fitting windows are tested from 0.3 to 1. For each fitting window, more than 3000 fitting trials are performed, starting with different initial fitting parameters. We

extract (F_c, ν, y, \vec{g}) by averaging over all the obtained global minima for all w and give the error bars by the standard deviation.

We mainly consider two situations, without correction and with the simplest first-order correction. When the correction is absent, i.e., $n_1 = 0$, there are only two fitting parameters (F_c, ν) . The global minima of $\mathcal{D}(F_c, \nu)$ for all the fitting windows at $\epsilon = 0.5$ are shown in Figs. 6(a) and 6(b). The loca of the minima for different fitting windows are tied together, thus the fluctuations of the critical points are quiet small.

When considering the simplest first-order correction by setting $n_1 = 1$ and $n_0 = 0$, there are four free fitting parameters (F_c, ν, y, g_{10}) . We note that small fluctuation in y would cause large fluctuation in g_{10} . The fitting regime of g_{10} is restricted to $[-10, 10]$. This restriction hardly influences (F_c, ν) , with (F_c, ν) changed within the error bars when magnifying this regime for ten times. Figures 6(c) to 6(f) show the minima for all the fitting windows at $\epsilon = 0.5$. We can see that the minima are bunched into two clusters, with the local minima framed in the dashed red box and global minima in the solid blue box. The locations of the local minima (F_c, ν) are consistent with those of the global minima in Figs. 6(a) and 6(b) where the correction is absent. This can be explained by the large values of the corresponding $|y|$, which makes the correction far less important. This correspondence also means that including the first-order correction will improve the degree of collapse by reducing \mathcal{D} . The global minima \mathcal{D}_{\min} at all ϵ with and without correction are shown in Fig. 6(g). For all ϵ , \mathcal{D}_{\min} is reduced with a magnitude less than one order when the simplest first-order correction is considered. The corrected data after subtraction of the correction are shown in Fig. 7, which corresponds to Fig. 3 without correction. We can see that after correction these curves for different system sizes now cross at fixed F_c .

- [1] P. W. Anderson, Absence of diffusion in certain random lattices, *Phys. Rev.* **109**, 1492 (1958).
- [2] N. F. Mott, M. Pepper, S. Pollitt, R. H. Wallis, and C. J. Adkins, The Anderson transition, *Proc. R. Soc. Lond. A* **345**, 169 (1975).
- [3] E. Abrahams, P. W. Anderson, D. C. Licciardello, and T. V. Ramakrishnan, Scaling Theory of Localization: Absence of

Quantum Diffusion in Two Dimensions, *Phys. Rev. Lett.* **42**, 673 (1979).

- [4] P. A. Lee and T. V. Ramakrishnan, Disordered electronic systems, *Rev. Mod. Phys.* **57**, 287 (1985).
- [5] S. S. Kondov, W. R. McGehee, J. J. Zirbel, and B. DeMarco, Three-dimensional anderson localization of ultracold matter, *Science* **334**, 66 (2011).

- [6] G. Semeghini, M. Landini, P. Castilho, S. Roy, G. Spagnoli, A. Trenkwalder, M. Fattori, M. Inguscio, and G. Modugno, Measurement of the mobility edge for 3D Anderson localization, *Nat. Phys.* **11**, 554 (2015).
- [7] C. M. Soukoulis and E. N. Economou, Localization in One-Dimensional Lattices in the Presence of Incommensurate Potentials, *Phys. Rev. Lett.* **48**, 1043 (1982).
- [8] D. J. Boers, B. Goedeke, D. Hinrichs, and M. Holthaus, Mobility edges in bichromatic optical lattices, *Phys. Rev. A* **75**, 063404 (2007).
- [9] J. Biddle, D. J. Priour, B. Wang, and S. Das Sarma, Localization in one-dimensional lattices with non-nearest-neighbor hopping: Generalized Anderson and Aubry-André models, *Phys. Rev. B* **83**, 075105 (2011).
- [10] S. Ganeshan, J. H. Pixley, and S. Das Sarma, Nearest Neighbor Tight Binding Models with an Exact Mobility Edge in One Dimension, *Phys. Rev. Lett.* **114**, 146601 (2015).
- [11] X. Li, X. Li, and S. Das Sarma, Mobility edges in one-dimensional bichromatic incommensurate potentials, *Phys. Rev. B* **96**, 085119 (2017).
- [12] H. P. Lüschen, S. Scherg, T. Kohlert, M. Schreiber, P. Bordia, X. Li, S. Das Sarma, and I. Bloch, Single-Particle Mobility Edge in a One-Dimensional Quasiperiodic Optical Lattice, *Phys. Rev. Lett.* **120**, 160404 (2018).
- [13] I. V. Gornyi, A. D. Mirlin, and D. G. Polyakov, Interacting Electrons in Disordered Wires: Anderson Localization and Low- T Transport, *Phys. Rev. Lett.* **95**, 206603 (2005).
- [14] D. M. Basko, I. L. Aleiner, and B. L. Altshuler, Metal-insulator transition in a weakly interacting many-electron system with localized single-particle states, *Ann. Phys. (NY)* **321**, 1126 (2006).
- [15] R. Nandkishore and D. A. Huse, Many-body localization and thermalization in quantum statistical mechanics, *Annu. Rev. Condens. Matter Phys.* **6**, 15 (2015).
- [16] D. A. Abanin, E. Altman, I. Bloch, and M. Serbyn, Colloquium: Many-body localization, thermalization, and entanglement, *Rev. Mod. Phys.* **91**, 021001 (2019).
- [17] D. J. Luitz, N. Laflorencie, and F. Alet, Many-body localization edge in the random-field Heisenberg chain, *Phys. Rev. B* **91**, 081103 (2015).
- [18] M. Serbyn, Z. Papić, and D. A. Abanin, Criterion for Many-Body Localization-Delocalization Phase Transition, *Phys. Rev. X* **5**, 041047 (2015).
- [19] M. Žnidarič, T. Prosen, and P. Prelovšek, Many-body localization in the Heisenberg XXZ magnet in a random field, *Phys. Rev. B* **77**, 064426 (2008).
- [20] J. H. Bardarson, F. Pollmann, and J. E. Moore, Unbounded Growth of Entanglement in Models of Many-Body Localization, *Phys. Rev. Lett.* **109**, 017202 (2012).
- [21] R. Vosk and E. Altman, Many-body localization in one dimension as a dynamical renormalization group fixed point, *Phys. Rev. Lett.* **110**, 067204 (2013).
- [22] M. Serbyn, Z. Papić, and D. A. Abanin, Universal slow growth of entanglement in interacting strongly disordered systems, *Phys. Rev. Lett.* **110**, 260601 (2013).
- [23] B. Bauer and C. Nayak, Area laws in a many-body localized state and its implications for topological order, *J. Stat. Mech.: Theory Exp.* (2013) P09005.
- [24] M. Serbyn, Z. Papić, and D. A. Abanin, Local Conservation Laws and the Structure of the Many-Body Localized States, *Phys. Rev. Lett.* **111**, 127201 (2013).
- [25] J. A. Kjäll, J. H. Bardarson, and F. Pollmann, Many-Body Localization in a Disordered Quantum Ising Chain, *Phys. Rev. Lett.* **113**, 107204 (2014).
- [26] V. Oganesyan and D. A. Huse, Localization of interacting fermions at high temperature, *Phys. Rev. B* **75**, 155111 (2007).
- [27] A. Pal and D. A. Huse, Many-body localization phase transition, *Phys. Rev. B* **82**, 174411 (2010).
- [28] E. Cuevas, M. Feigel'man, L. Ioffe, and M. Mezard, Level statistics of disordered spin-1/2 systems and materials with localized Cooper pairs, *Nat. Commun.* **3**, 1128 (2012).
- [29] J. Smith, A. Lee, P. Richerme, B. Neyenhuis, P. W. Hess, P. Hauke, M. Heyl, D. A. Huse, and C. Monroe, Many-body localization in a quantum simulator with programmable random disorder, *Nat. Phys.* **12**, 907 (2016).
- [30] S. S. Kondov, W. R. McGehee, W. Xu, and B. DeMarco, Disorder-Induced Localization in a Strongly Correlated Atomic Hubbard Gas, *Phys. Rev. Lett.* **114**, 083002 (2015).
- [31] J. Y. Choi, S. Hild, J. Zeiher, P. Schauß, A. Rubio-Abadal, T. Yefsah, V. Khemani, D. A. Huse, I. Bloch, and C. Gross, Exploring the many-body localization transition in two dimensions, *Science* **352**, 1547 (2016).
- [32] M. Schreiber, S. S. Hodgman, P. Bordia, H. P. Lüschen, M. H. Fischer, R. Vosk, E. Altman, U. Schneider, and I. Bloch, Observation of many-body localization of interacting fermions in a quasirandom optical lattice, *Science* **349**, 842 (2015).
- [33] P. Bordia, H. Lüschen, S. Scherg, S. Gopalakrishnan, M. Knap, U. Schneider, and I. Bloch, Probing Slow Relaxation and Many-Body Localization in Two-Dimensional Quasiperiodic Systems, *Phys. Rev. X* **7**, 041047 (2017).
- [34] H. P. Lüschen, P. Bordia, S. Scherg, F. Alet, E. Altman, U. Schneider, and I. Bloch, Observation of Slow Dynamics near the Many-Body Localization Transition in One-Dimensional Quasiperiodic Systems, *Phys. Rev. Lett.* **119**, 260401 (2017).
- [35] P. Roushan, C. Neill, J. Tangpanitanon, V. M. Bastidas, A. Megrant, R. Barends, Y. Chen, Z. Chen, B. Chiaro, A. Dunsworth, A. Fowler, B. Foxen, M. Giustina, E. Jeffrey, J. Kelly, E. Lucero, J. Mutus, M. Neeley, C. Quintana, D. Sank, A. Vainsencher, J. Wenner, T. White, H. Neven, D. G. Angelakis, and J. Martinis, Spectroscopic signatures of localization with interacting photons in superconducting qubits, *Science* **358**, 1175 (2017).
- [36] K. Xu, J. J. Chen, Y. Zeng, Y. R. Zhang, C. Song, W. Liu, Q. Guo, P. Zhang, D. Xu, H. Deng, K. Huang, H. Wang, X. Zhu, D. Zheng, and H. Fan, Emulating Many-Body Localization with a Superconducting Quantum Processor, *Phys. Rev. Lett.* **120**, 050507 (2018).
- [37] K. X. Wei, C. Ramanathan, and P. Cappellaro, Exploring Localization in Nuclear Spin Chains, *Phys. Rev. Lett.* **120**, 070501 (2018).
- [38] M. Rispoli, A. Lukin, R. Schittko, S. Kim, M. E. Tai, J. Léonard, and M. Greiner, Quantum critical behavior at the many-body localization transition, *Nature (London)* **573**, 385 (2019).
- [39] A. Lukin, M. Rispoli, R. Schittko, M. E. Tai, A. M. Kaufman, S. Choi, V. Khemani, J. Léonard, and M. Greiner, Probing entanglement in a many-body-localized system, *Science* **364**, 256 (2019).

- [40] M. Schulz, C. A. Hooley, R. Moessner, and F. Pollmann, Stark Many-Body Localization, *Phys. Rev. Lett.* **122**, 040606 (2019).
- [41] E. van Nieuwenbrug, Y. Baum, and G. Refael, From Bloch oscillations to many-body localization in clean interacting systems, *Proc. Natl. Acad. Sci. U.S.A.* **116**, 9269 (2019).
- [42] S. R. Taylor, M. Schulz, F. Pollmann, and R. Moessner, Experimental probes of Stark many-body localization, *Phys. Rev. B* **102**, 054206 (2020).
- [43] L.-N. Wu and A. Eckardt, Bath-Induced Decay of Stark Many-Body Localization, *Phys. Rev. Lett.* **123**, 030602 (2019).
- [44] T. Chanda, R. Yao, and J. Zakrzewski, Coexistence of localized and extended phases: Many-body localization in a harmonic trap, *Phys. Rev. Research* **2**, 032039(R) (2020).
- [45] G. H. Wannier, Wave functions and effective hamiltonian for bloch electrons in an electric field, *Phys. Rev.* **117**, 432 (1960).
- [46] G. H. Wannier, Dynamics of band electrons in electric and magnetic fields, *Rev. Mod. Phys.* **34**, 645 (1962).
- [47] H. Fukuyama, R. A. Bari, and H. C. Fogedby, Tightly bound electrons in a uniform electric field, *Phys. Rev. B* **8**, 5579 (1973).
- [48] Y. Y. Atas, E. Bogomolny, O. Giraud, and G. Roux, Distribution of the Ratio of Consecutive Level Spacings in Random Matrix Ensembles, *Phys. Rev. Lett.* **110**, 084101 (2013).
- [49] K. Slevin and T. Ohtsuki, Corrections to Scaling at the Anderson Transition, *Phys. Rev. Lett.* **82**, 382 (1999).
- [50] A. Rodriguez, L. J. Vasquez, K. Slevin, and R. A. Römer, Multifractal finite-size scaling and universality at the Anderson transition, *Phys. Rev. B* **84**, 134209 (2011).
- [51] D. S. Bhakuni and A. Sharma, Entanglement and thermodynamic entropy in a clean many-body-localized system, *J. Phys.: Condens. Matter* **32**, 255603 (2020).
- [52] T. Orito, Y. Kuno, and I. Ichinose, Topological order versus many-body localization in periodically modulated spin chains, *Phys. Rev. B* **100**, 214202 (2019).
- [53] Q. Guo, C. Cheng, Z.-H. Sun, Z. Song, H. Li, Z. Wang, W. Ren, H. Dong, D. Zheng, Y.-R. Zhang, R. Mondaini, H. Fan, and H. Wang, Observation of energy-resolved many-body localization, *Nat. Phys.* **17**, 234 (2021).
- [54] M. White, M. Pasienski, D. McKay, S. Q. Zhou, D. Ceperley, and B. DeMarco, Strongly Interacting Bosons in a Disordered Optical Lattice, *Phys. Rev. Lett.* **102**, 055301 (2009).
- [55] S. Q. Zhou and D. M. Ceperley, Construction of localized wave functions for a disordered optical lattice and analysis of the resulting Hubbard model parameters, *Phys. Rev. A* **81**, 013402 (2010).
- [56] G. J. A. Edge, R. Anderson, D. Jervis, D. C. McKay, R. Day, S. Trotzky, and J. H. Thywissen, Imaging and addressing of individual fermionic atoms in an optical lattice, *Phys. Rev. A* **92**, 063406 (2015).
- [57] L. W. Cheuk, M. A. Nichols, M. Okan, T. Gersdorf, V. V. Ramasesh, W. S. Bakr, T. Lompe, and M. W. Zwierlein, Quantum-Gas Microscope for Fermionic Atoms, *Phys. Rev. Lett.* **114**, 193001 (2015).
- [58] M. F. Parsons, F. Huber, A. Mazurenko, C. S. Chiu, W. Setiawan, K. Wooley-Brown, S. Blatt, and M. Greiner, Site-Resolved Imaging of Fermionic ${}^6\text{Li}$ in an Optical Lattice, *Phys. Rev. Lett.* **114**, 213002 (2015).
- [59] E. Haller, J. Hudson, A. Kelly, D. A. Cotta, B. Peaudecerf, G. D. Bruce, and S. Kuhr, Single-atom imaging of fermions in a quantum-gas microscope, *Nat. Phys.* **11**, 738 (2015).
- [60] A. Omran, M. Boll, T. A. Hilker, K. Kleinlein, G. Salomon, I. Bloch, and C. Gross, Microscopic Observation of Pauli Blocking in Degenerate Fermionic Lattice Gases, *Phys. Rev. Lett.* **115**, 263001 (2015).
- [61] R. Yao and J. Zakrzewski, Many-body localization of bosons in optical lattice: Dynamics in disorder-free potentials, *Phys. Rev. B* **102**, 104203 (2020).